Journal of Neuroscience Methods 141 (2005) 321–332

JOURNAL OF NEUROSCIENCE METHODS

www.elsevier.com/locate/jneumeth

A statistically based density map method for identification and quantification of regional differences in microcolumnarity in the monkey brain

Luis Cruz[a,*], Sergey V. Buldyrev[a], Shouyong Peng[a], Daniel L. Roe[b], Brigita Urbanc[a], H.E. Stanley[a,1], Douglas L. Rosene[b,c]

[a] *Department of Physics, Center for Polymer Studies, Boston University, 590 Commonwealth Ave, Boston, MA 02215, USA*
[b] *Department of Anatomy and Neurobiology, Boston University School of Medicine, Boston, MA 02118, USA*
[c] *Yerkes National Primate Research Center, Emory University, Atlanta, GA 30322, USA*

Received 8 June 2004; received in revised form 9 September 2004; accepted 17 September 2004

Abstract

We present a statistical density map method derived from condensed matter physics to quantify microcolumns, the fundamental computational unit of the cerebral cortex. This method provides measures for microcolumnar strength, width, spacing, length, and periodicity. We applied this method to Nissl-stained 30 μm thick frozen sections from areas 46, TE, and TL of rhesus monkey brains, areas that differ visually in microcolumnarity and are associated with different cognitive functions. Our results indicate that microcolumns in these areas are similar in width, spacing, and periodicity, but are stronger (possess a higher neuronal density) in area TE, as compared to areas TL and 46. We modeled the effect of section orientation on microcolumnar spacing and demonstrated that this method provides an adequate estimate of spacing. We also modeled disruption of microcolumnarity by performing simulations that randomly displace neurons and demonstrated that displacements of only one neuronal diameter effectively eliminate microcolumnar organization. These results indicate that our density map method is sensitive enough to detect and quantify subtle differences in microcolumnar organization that may occur in the context of development, aging, and neuropathology, as well as between areas and species.

Keywords: Microcolumns; Cerebral cortex; Primate brain; Modeling; Correlation; Neuronal organization

1. Introduction

The most prominent feature of cortex is the arrangement of neurons into layers with classical "neocortex" identified as having six layers. Because these layers differ in thickness, cell type, and cell density from one part of the cortex to another, these "laminar" differences have been used to subdivide the cortex into different regions (e.g. Brodmann, 1909; Vogt and Vogt, 1919; von Economo and Koskinas, 1925; Von Bonin and Bailey, 1947; Petrides and Pandya, 1994). It has also been noted that different cortical regions display a "vertical" organization of neurons grouped into columnar arrangements that take two forms: macrocolumns, approximately 0.4–0.5 mm in diameter (Mountcastle, 1957; Calvin, 1995), and microcolumns or minicolumns approximately 30 μm in diameter (Jones, 2000).

Macrocolumns were first identified functionally by Mountcastle (1957), who described groups of neurons in somatosensory cortex that respond to light touch alternating with laterally adjacent groups that respond to joint and/or muscle stimulation. These groups form a mosaic with a

* Corresponding author. Tel.: +1 617 353 3411; fax: +1 617 353 3783.
E-mail addresses: ccruz@bu.edu (L. Cruz), sergey@argento.bu.edu (S.V. Buldyrev), shypeng@argento.bu.edu (S. Peng), dlroe@bu.edu (D.L. Roe), brigita@bu.edu (B. Urbanc), hes@bu.edu (H.E. Stanley), drosene@bu.edu (D.L. Rosene).
URL: http://polymer.bu.edu/cruz (L. Cruz), http://polymer.bu.edu/hes (H.E. Stanley).
[1] Tel.: +1 857 891 1941 (cell). +1 617 353 2617 (off.); fax: +1 617 353 3783.

0165-0270/$ – see front matter © 2004 Elsevier B.V. All rights reserved.
doi:10.1016/j.jneumeth.2004.09.005

periodicity of about 0.5 mm. Similarly, Hubel and Wiesel (1963, 1969, 1977) using both monkeys and cats discovered alternating macrocolumns of neurons in the visual cortex that respond preferentially to the right or to the left eye. These "ocular dominance columns" have a spacing of about 0.4 mm. In addition, they discovered within the ocular dominance columns smaller micro- or mini-columns of neurons that respond preferentially to lines in a particular orientation.

Once these physiological minicolumns were recognized, it was noted that vertically organized columns of this approximate size are visible in many cortical areas under low magnification and are composed of perhaps 100 neurons stretching from layer V through layer II. To prove that the physiological and morphologically defined minicolumns or microcolumns are identical to the physiologically defined minicolumn would require directly measuring the response of a majority of the neurons in a single histologically identified microcolumn, but this has yet to be done. Nevertheless, current data on the microcolumn indicate that the neurons within the microcolumn receive common inputs, have common outputs, are interconnected, and may well constitute a fundamental computational unit of the cerebral cortex (e.g. Szentagothai, 1975; Swindale, 1990; Purves et al., 1992; Saleem et al., 1993; Van Hoesen and Solodkin, 1993; Buxhoeveden et al., 1996; Mountcastle, 1997; Buxhoeveden and Casanova, 2002a,b; Mountcastle, 2003). These microcolumns vary in spacing across the cortex and species, but are about 30 μm apart in human visual cortex (Calvin, 1995).

The microcolumn has recently been shown to be disrupted in a number of different conditions including Alzheimer's Disease (AD) and Lewy Body dementia (LBD) (Buldyrev et al., 2000), autism (Casanova et al., 2002a), dyslexia (Casanova et al., 2002b), and schizophrenia (Buxhoeveden et al., 2000b). Interestingly, in normal aging monkeys where cortical neurons are largely preserved (e.g. Peters et al., 1998) there is evidence of age-related functional disruption of orientation selectivity in the visual cortex of aged monkeys (Schmolesky et al., 2000; Leventhal et al., 2003). In these studies, Leventhal and colleagues reported a loss of two functional properties of microcolumns—orientation and direction selectivity. Moreover, they demonstrated that administration of GABA agonists restored these functions. Since the small GABAergic interneurons are important components of the microcolumn, this suggests that there may well be a disruption of at least this or a related component of the microcolumn in normal aging.

While structural and functional disruption of microcolumns in neuropathological conditions and in normal aging is extremely interesting, because of the lack of highly efficient analytical methods, these observations have been confined to a few selected regions in each condition and have not been well-studied across wide areas of the brain, in development and normal aging, or across many species.

To facilitate investigations of microcolumns, quantitative methods that can be applied efficiently and reliably to obtain statistically valid measures of microcolumnarity in standard histological preparations of post-mortem brains from humans and laboratory animals are required. To achieve this, we have adapted our density map method (Buldyrev et al., 2000) to characterize the degree of microcolumnarity by quantifying microcolumnar strength (i.e. neuronal density along the microcolumn), microcolumnar width, length and periodicity, and distance between microcolumns. This allows the degree of microcolumnarity to be compared between different cytoarchitectonic regions within a brain, between the same cytoarchitectonic regions across different experimental conditions (e.g. development, aging, neurodegenerative diseases), and to be correlated directly with physiological studies in the same subjects. In this paper, we have applied this method to characterize three different cortical areas in the rhesus monkey brain and have validated the method against direct tissue measurements. The strength of our method lies in the ability to characterize microcolumnar parameters that will allow straightforward statistical comparisons between areas or species, between normal and diseased brains, or across the lifespan.

2. Methods

2.1. Subjects

Brain tissue was obtained from three young adult female rhesus monkeys (ranging in age from 6.4 to 6.7 years) that were part of an ongoing study of the effects of aging on cognitive function. Animals were housed in the Laboratory Animal Science Center of Boston University Medical Center that is fully accredited by the Association for the Assessment and Accreditation of Laboratory Animal Care. All procedures were approved by the Institutional Animal Care and Use Committee of Boston University Medical Center and conformed to the NIH *Guide for the Care and Use of Laboratory Animals* and the U.S. *Public Health Service Policy on Humane Care and Use of Laboratory Animals*. After MRI scanning to ensure there was no occult pathology in the brain and behavioral testing to assess cognitive function (e.g. Herndon et al., 1997), monkeys were tranquilized with ketamine hydrochloride (10 mg/kg), deeply anesthetized with sodium pentobarbital (up to 20 mg/kg to effect), and killed by exsanguination during transcardial perfusion of the brain with 4 liters of warm (37 °C) fixative containing either 4% paraformaldehyde alone or a mixture of 1% paraformaldehyde and 1.25% glutaraldehyde in 0.1 M phosphate buffer (pH 7.4). Immediately after perfusion fixation of the brain, the cranium was opened and the brain was blocked, in situ, in the coronal stereotactic plane. One hemisphere was then cryoprotected in graded solutions culminating with 20% glycerol and 2% DMSO in phosphate buffer (0.1 M, pH 7.4) after which the blocks were flash frozen by immersion in −75 °C isopentane (Rosene et al., 1986). All blocks were stored in an ultralow freezer at −80 °C until cut.

2.2. Tissue processing

Frozen blocks were oriented on the freezing stage of a sledge microtome and sections were cut in the coronal stereotactic plane into eight interrupted series of 30 μm thick sections and one series of 60 μm thick sections so that sections in each series were spaced 300 μm apart. A 30 μm thick series was mounted on microscope slides allowed to dry overnight and then stained with thionin, dehydrated, cleared, and coverslipped.

Since the sections adhere rapidly to the subbed surface of the slide before they dry, this method preserves the *XY* relationships within the section. However, as the section dries, it shrinks in the *Z* dimension (thickness) from the originally cut thickness of 30 μm to an average mounted section thickness of about 8–10 μm, as determined using the Bioquant Image Analysis system equipped with a Heidenhain stage microcrometer that measures the *Z* axis position to 0.1 μm.

2.3. Cytoarchitectonic regions to be studied

For this study, three cortical regions that are all implicated in distinct cognitive functions and which visually differ in the degree of microcolumnarity were selected for analysis. These are: (i) area 46 of the prefrontal cortex (PFC) in the lower bank of sulcus principalis, (ii) area TE of the inferior temporal region immediately below the superior temporal sulcus, and (iii) area TL of the parahippocampal gyrus a few millimeters medial to the occipitotemporal sulcus. Area TE is a neocortical region with striking "columnarity" that is involved in visual object recognition (Tsao et al., 2003; Tanaka, 2003). Area 46 is a neocortical region implicated in working memory and executive functions (Goldman and Rosvold, 1970; Goldman et al., 1971; Goldman-Rakic, 1988; Petrides, 2000a,b; Moore et al., 2002, 2003) that has an intermediate degree of columnarity. Area TL is a proisocortical region involved in recognition memory (e.g. Damasio et al., 1982; Suzuki, 1996; Blatt and Rosene, 1998; Blatt et al., 2003) that has little visual evidence of microcolumns.

2.4. Digital photography

Sections were selected from two levels matched across all cases: (i) the prefrontal cortex in the middle of the back third of the sulcus principalis containing area 46 (Petrides and Pandya, 1994), and (ii) the temporal lobe at the level of the lateral geniculate nucleus containing area TE on the lateral surface and area TL (e.g. Blatt et al., 2003) on the ventral surface. Photomicrographs spanning layers II–IV were taken at 10× objective magnifications on a Nikon E600 microscope equipped with a high resolution digital camera and used as input to the semi-automated neuron recognition program described below. We restricted our analysis to neurons in layer III for several reasons. First, the moderate density and relative size of neurons in layer III facilitates the semi-automated distinction of neurons from glia, as described below. Second, layer III is easily defined in each of the chosen regions facilitating reliable sampling of a comparable area. Third, layer III has approximately similar neuronal densities across the three regions (as confirmed in the results) facilitating the interpretation that differences in columnarity reflect different spatial organization and not just different packing densities. Future efforts will examine microcolumns in layer IV which has vastly different densities across the regions and layer V which has much lower densities in all three areas.

2.5. Manual Identification of XY coordinates for neurons and glia

Using the digital images, two neurons at diagonally opposed ends of the image were identified at the 10× objective magnification with the Bioquant Image Analysis System and marked as fiducials for alignment with the semi-automated identification map. Then, using the 60× objective, every neuron and every glia cell was separately marked throughout the image. This yielded files containing the *XY* coordinates of every neuron and every glia cell visually identified for later comparison with the *XY* coordinates derived by our semi-automated detection method.

2.6. Semi-automated detection of XY coordinates for neurons

To generate the large pool of *XY* coordinate data necessary for our density maps, we developed a method to semi-automatically locate neurons within the digitized images. This method uses the relative darkness of the cell body (dense quasi-circular shape) and its size to distinguish neurons from glia, blood vessels, and endothelial cells. This method consists of: (i) applying a wavelet transform filter (pre-processing), (ii) marking all regions that are locally darker (preliminary candidates), and (iii) choosing those markings that are surrounded by enough dark area over a neuronal radius (final selection). Step (i), the wavelet filter, has the effect of de-emphasizing features smaller and larger than a given input length parameter, and to enhance all structures of comparable dimension as this length parameter. This length parameter is manually adjusted so that the filter enhances neurons while discarding smaller objects such as glial cells and bigger structures such as blood vessels. The range of values used is between 8 and 16 μm, which is of the same order as a typical neuronal diameter. Next, in step (ii) we find the positions of the local "darkest" points (local maxima). These are the most likely positions for neurons, but may contain false positives. The false positives are filtered out in step (iii) by using an algorithm that examines the neighborhood enclosed by a circle of a radius of value chosen to be the average neuronal radius, and that calculates the average darkness level inside this circle in order to compare and select only those neighborhoods that "look" like typical neuronal bodies. It is this last step (iii) that imposes the size and neuronal "body" (darkness) criteria for the final selection of

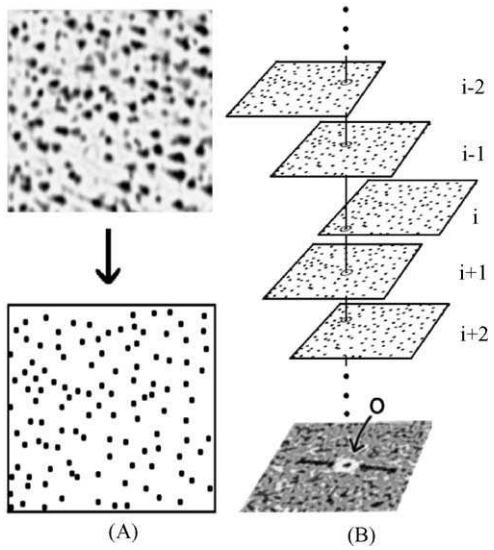

Fig. 1. Illustration of the density map calculation. (A) Starting from a digitized image (upper), neuronal coordinates are identified (lower). (B) For each neuron *i*, an identical copy of the coordinate image is made. All images are then translated and superimposed so that the circled neurons (. . .*i* − *1*, *i*, *i* + *1*. . .) line up with the origin at *O*. Because each coordinate image contributes to the density map with equal weight (bottom of (B)), the density map effectively represents the average neighborhood of a neuron.

neuronal locations (Fig. 1A). Supplementary information as well as detailed pictures illustrating this method are available at http://polymer.bu.edu/cruz/export/060404.

2.7. Density map method

The density map method has been described elsewhere (Buldyrev et al., 2000). Briefly, by using as input *XY* neuronal coordinates obtained from either direct manual detection or any available semi-automated detection method, the density map method calculates the density correlation function, $g(x,y)$, that describes the average neighborhood (neuronal density) surrounding a neuron in the cortex. We first assign indices ($i = 1,2,3\ldots N$) to all the neurons in the sample that have been detected (Fig. 1A). Next, we create N copies of the image and superimpose all of these images, one on top of each other (Fig. 1B), with each image shifted (without rotation) on the superposition plane so that one identified neuron i (one per plane) sits on top of a reference origin O (Fig. 1B, bottom). We then flatten all of the layers in the superposition to create a single two-dimensional image over which we place a grid, with grid spacing D, and count the number of neurons $m(x,y)$ in each grid cell. We define $g(x,y) = m(x,y)/ND^2$, in which $g(x,y)$ has units of an average density of objects at position (x,y). Plotting the value of $g(x,y)$ for each position results in a two-dimensional topographical map in which the value of $g(x,y)$ is represented by shades of gray, where darkness is proportional to neuronal density. Visually, the resulting density map is homogenous if locations of objects (neurons) are uncorrelated, but will show patterns if there are any regular spatial arrangements between them. Individual density maps derived from adjacent fields (photomicrographs) are averaged together in order to obtain one density map per cytoarcitectonic region. However, since from one field to another the angular orientation of the microcolumns varies (less than 20°), the individual maps are rotated so that the vertical axis of each density map is aligned before they are averaged.

2.8. Quantification of density maps

Once we calculate $g(x,y)$ for a particular region of interest (ROI), we quantify any microcolumnar structure by extracting the following measures:

- W, microcolumnar width,
- P, distance between microcolumns,
- L, length of microcolumns,
- S, strength of microcolumns, defined as the ratio of the neuronal density within a microcolumn to the average neuronal density,
- T, degree of microcolumnar periodicity, defined as the ratio of the neuronal density of neighboring microcolumns to the average neuronal density.

The width W of the central column and the distance between the central column and the nearest neighboring column P are obtained by first plotting the intensity of the density map within the horizontal white lines shown in Fig. 2A. These lines are perpendicular to the microcolumn and intersect it not at the center ($x = 0, y = 0$), but at a location below (or symmetrically above) the center ($x = 0, y = \pm 2R$; where R is of the order of a neuronal radius), as shown. From this intensity plot (Fig. 2B) W is defined as the width of its central peak at the value of the average density (horizontal thin line in Fig. 2B) and P is defined as the average distance between the central peak and the nearest peaks. The length L of microcolumns is obtained by similarly plotting the intensity along the vertical and fitting this plot with an exponential curve of the form $A + B\exp(-y/L)$, where y has a range $y > 2R$ (i.e. discarding the center), and A, B, and L are the fitting parameters to the plot. The strength S and degree of microcolumnar periodicity T are defined as a ratio of two local neuronal densities, ρ, at locations 1 and 5 (marked in Fig. 2C), and the average neuronal density ρ_{ave}. Thus, the strength is defined as $S = \rho(1)/\rho_{ave}$ and the degree of periodicity as $T = \rho(5)/\rho_{ave}$. A high (low) S will reflect an increased (decreased) probability of finding a neuron along the vertical extent of the microcolumn. Also, a high (low) T will indicate that there is a strong (weak) degree of periodicity. At location 3 in Fig. 2C, the value of ρ corresponds to the average number of neurons at the origin, which by definition is $\rho = g(0,0) = 1/D^2$. The densities at locations 2 and 4 are small in comparison with ρ_{ave} because neurons are not likely to occupy this adjacent space due to their mutual mass exclusion (i.e. two objects cannot occupy the same position in space), and are therefore not reported here.

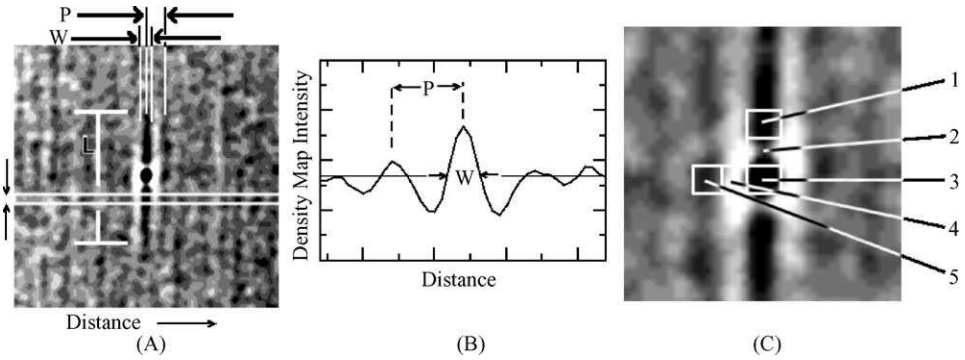

Fig. 2. Quantification of density maps. (A) Density maps calculated from samples with microcolumnar organization exhibit a vertical columnar structure characterized by width *W*, separated from neighboring microcolumns by a distance *P*, and of length *L*. (B) *W* and *P* are obtained by plotting the intensity of the density map within the horizontal strips shown in (A), in which *P* is the distance between peaks and *W* is the width of the central peak measured at the average neuronal density (ρ_{ave}, thin horizontal line in (B)). (C) Density maps of microcolumns have an anisotropic distribution of neuronal density in the locality of the neuron at the origin. We measure the neuronal density ρ at the: (1) vertical intra-column region, (2) intra-inter-columnar depleted regions (4) inter-columnar depleted regions, (3) origin, and (5) neighbor column region. The microcolumnar strength *S* is defined as $\rho(1)/\rho_{ave}$ and the degree of microcolumnar periodicity *T* as $\rho(5)/\rho_{ave}$.

2.9. Validation of semi-automated neuronal detection

To validate the semi-automated detection of neurons, we compared neuronal identifications from both manual and semi-automated detection performed on identical digital images of tissue and obtained four quantities: the total number of manually marked neurons S_T, the number of neurons correctly identified in the semi-automated method S_i, the number of non-neuronal objects incorrectly identified as neurons in the semi-automated method S_o, and the total number of objects identified semi-automatically as neurons $S_d = S_i + S_o$. We define the accuracy (sensitivity) of the semi-automated detection by S_i/S_T and the relative error by S_o/S_d. We note that the sum of the accuracy plus the error can be greater than 1.0 since the semi-automated detection can yield more objects than the number of manually marked neurons. Results of these quantities are reported in Section 3.3.

3. Results

3.1. Neuronal selection and counts

We analyzed two 30 μm thick Nissl-stained sections spaced 300–600 μm apart at each of the matched levels across all three cases. For each section, we acquired four adjacent (non-overlapping) 10× images of layer III, each with an area of 342 μm × 342 μm. Thus, we analyzed a total of $3 \times 2 \times 4 = 24$ images per architectonic area in each of the three cases for a total of 72 images. While the microcolumns extend from layer V up into layer II, we restricted our analysis to neurons in layer III as described in the Section 2. For each area, the total count of semi-automatically detected neurons as well as total area of tissue analyzed are reported in Table 1 and demonstrates that the average neuronal density (last column of Table 1) is nearly the same for all areas.

3.2. Density map quantifications

The resulting density maps for the cases described above are shown in Fig. 3. These maps retain the same scale as the original photomicrographs and the "darkness" is proportional to the density of neurons at that position. The most striking feature in these three density maps is the very distinct column at the origin of the map, which represents the average structure of microcolumns. The measures *L*, *W*, and *P* are readily calculated directly from these maps (following Fig. 2A and B and Section 2.8). For *S* and *T* we first need to calculate the corresponding local neuronal densities at locations 1 and 5, respectively (Fig. 2C). Considering *S*, in Fig. 4 we show the density of neurons as a function of the vertical distance along the microcolumns in which the shaded area is proportional to $\rho(1)$. The graphs in Fig. 4 are obtained by first measuring the neuronal density within a thin vertical strip running in the vertical direction from top to bottom, wide enough to contain the microcolumn (about 8 μm). Secondly, we set our origin at $x = 0, y = 0$ of the density map, split the neuronal density within the vertical strip in an "up" and "down" direction (relative to the center), and average both directions to plot them in Fig. 4 for each area. The thin horizontal lines in each graph correspond to the average neuronal density for each area (Table 1). Using Fig. 4, we calculate *S* by integrating each curve between the positions marked by dashed vertical lines (between 15 and 40 μm from the origin) obtaining the shaded area, and then dividing by $\rho_{ave} \times 25$ μm. For *T*, we

Table 1
Neuronal selection and count

	Images	Neurons (detected objects)	Area (mm^2)	Average density (neurons/μm^2)
TL	24	3652	2.740	0.0013 ± 0.0003
46	24	3638	2.695	0.0013 ± 0.0003
TE	24	3763	2.741	0.0014 ± 0.0003

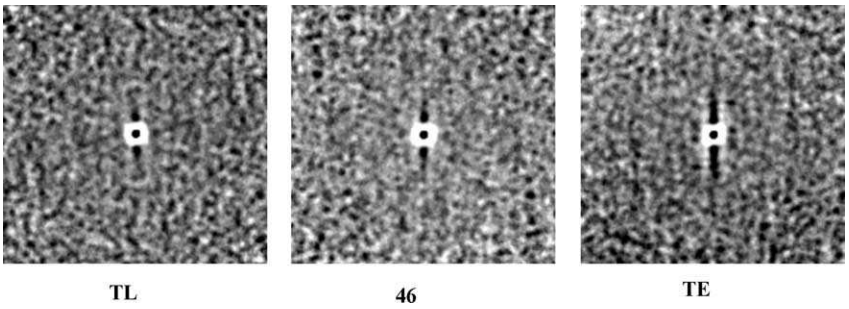

Fig. 3. Averaged density maps for each of the areas analyzed. The central dot is the neuron at the origin. The central vertical columnar region indicates a higher probability of finding neurons up and down the neurons at the origin, and the white surrounding area is the low probability of finding neurons due to mass exclusion, i.e. neurons cannot overlap. Microcolumnar structure decays rapidly with distance from the origin, particularly in the lateral direction.

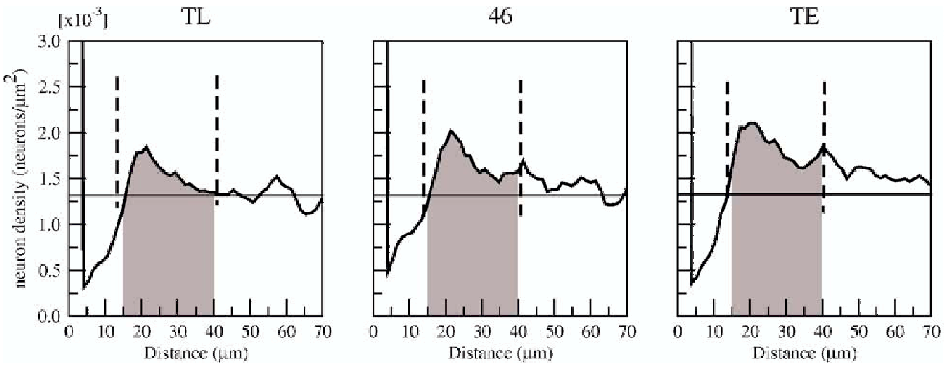

Fig. 4. Neuronal density along the microcolumn for each of the areas analyzed. The curves are calculated by measuring the intensity of the density map inside an 8 μm thick strip along the microcolumn. All of the curves are centered at the reference neuron of the density map. The dashed lines indicate the boundaries of region 1, as defined in Fig. 2C and the integral of the curve between them (shaded) is proportional to the local neuronal density $\rho(1)$. The ubiquitous first peak located at about 20 μm from the origin indicates a characteristic distance between nearest neighbor neurons along the vertical axis in the microcolumn.

perform the same neuronal density analysis as for *S*, but now in the horizontal direction perpendicular to the microcolumns (Fig. 2A), obtaining the cross sectional neuronal density defined in Fig. 2B (results not shown). Similarly to above, the integral of the curve within the first peak is $\rho(5)$, which divided by ρ_{ave}, corresponds to the degree of microcolumnar periodicity *T*.

The results for the measures from these density maps are summarized in Table 2 and plotted in Fig. 5. Results for *W*, *P*, and *T* do not show any appreciable difference when comparing the different areas as opposed to *S* and *L* which do show differences. However, while *L* shows a significant difference between TL and TE, differences in *S* are only marginally significant. In addition, *S* and *T* show contrasting behavior, in which strong *S* in all areas implies strong microcolumnarity, while small *T* ($T \sim 1$) means that there is a marginal degree of microcolumnar periodicity ($\rho(5) \approx \rho_{ave}$). If neighboring columns were placed at strictly regular intervals from each other, then *T* would have values much greater than 1. Re-

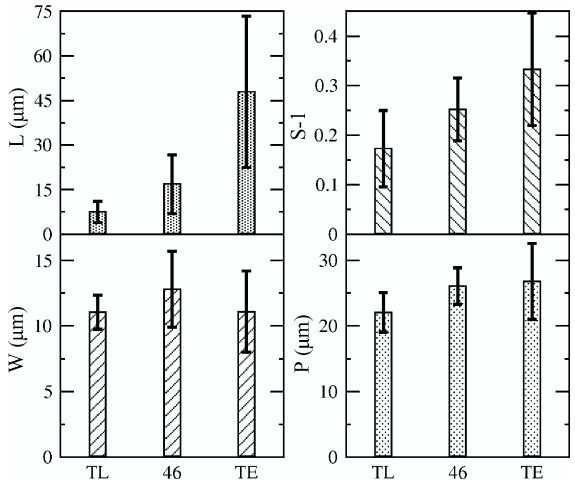

Fig. 5. Results for the measures of columnarity *L*, *S*, *W*, and *P*. The results were calculated from density maps using *XY* neuronal positions acquired from regions TL, 46, and TE. The error bars represent the respective standard deviations.

Table 2
Density map quantifications

	W (μm)	*P* (μm)	*L* (μm)	*S*	*T*
TL	11.1 ± 1.3	22.1 ± 3.0	7.5 ± 3.6	1.17 ± 0.08	1.04 ± 0.02
46	12.8 ± 2.9	26.1 ± 2.8	16.9 ± 9.9	1.25 ± 0.06	1.04 ± 0.03
TE	11.1 ± 3.1	26.8 ± 5.8	48.0 ± 25.5	1.33 ± 0.11	0.96 ± 0.06

garding error bars, we expect that analyzing a larger number of cases (more than the three analyzed here) will make significant the differences in *S*. Other features may also show significant differences, for example, the decrease in *P* from area TE to TL.

3.3. Validation of the approach

We validated the semi-automated neuronal detection by manually marking and recording positions of neurons in a small but sufficient number of images (four from area 46 and two from area TE), and compared these markings with neuronal detections using our semi-automated method. Averaging the results from each of the side-by-side comparisons, we obtained for the total number of manually marked neurons per image, $S_T = 122 \pm 24$, the number of correctly identified neurons per image, $S_i = 106 \pm 21$, with the total number of detected objects per image, $S_d = 136 \pm 32$. This gives an accuracy of $S_i/S_T \approx 0.87$ (i.e. more than 87% success in detecting neurons) with a relative error of $S_o/S_d \approx 0.22$ (i.e. of all the detected objects, about 22% are non-neuronal). Regarding the extent to which glial cell are miscounted among our detected objects, we offer the following argument. Considering that the non-neuronal objects counted in S_o may be, to a large extent, glial cells, we can write $S_g \approx S_o + qS_g$, where S_g is the number of glial cells, S_o is approximately the number of miscounted glial cells, and qS_g is the fraction of glial cells discarded by the method. In addition, because in a given image of these cortical areas there are approximately as many glial cells as neuronal bodies, then $S_g \approx S_T$. Combining these two relations we get $q \approx 1 - (S_d - S_i)/S_T$, which gives $q \approx 0.75$ when using the numbers above. This means that at least 75% of glial cells are discarded by our semi-automated recognition method.

To validate measures obtained from density maps using semi-automatically detected neurons as input, we compare these measures with those calculated using manually marked neurons from the same set of all available images from area TE. We show the resulting density maps side by side in Fig. 6, in which the qualitative similarities between the two

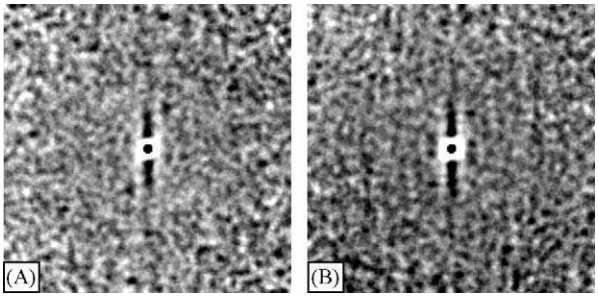

Fig. 6. Density maps calculated using *XY* neuronal positions from manual markings (A) and from applying the semi-automatic method to detect neurons (B). Both sets of *XY* neuronal positions were derived from the same digitized tissue images.

are evident. By comparing the quantitative measures of microcolumnarity, we confirmed that both density maps agree within error for *L*, *W*, *P*, *S*, and *T*.

3.4. Relative stability of microcolumns

As an exploration of the sensitivity of the measures of microcolumnarity presented above to changes in microcolumns across development, aging, or various neuropathological conditions as a result of subtle disruptions in the spatial position of neurons, we conducted a test to assess the degree of spatial disruption sufficient to alter our measures of microcolumnarity. Using a computer simulation and our own data, we allowed the positions of neurons to change in a controlled fashion. First, we selected one of the digitized images used for density map analysis from area TE, in which there were visually detectable microcolumns (shown on the left in Fig. 7). Second, we detected neurons in the field (top of Fig. 7A [$t = 0$]) and then generated a density map in the usual way (Fig. 7B). Third, we subjected all of the neuronal coordinates to change under the rules of Brownian motion, that is, the neurons were moved in random directions for *t* steps (Fig. 7C [$t = 300$]) using an average step size of 0.3 μm. A total of 300 steps were chosen so that the mean displacement of neurons would not exceed one neuronal diameter (in the neighborhood of 10 μm). After this procedure, a new density map was generated from the resulting *XY* coordinates of the neurons (Fig. 7D). The density map at $t = 0$ shows microcolumnarity (i.e. before the random displacement) while at $t = 300$ the measures of microcolumnarity are greatly reduced (are indistinguishable from a random system). We repeated these calculations for two other images (not shown) with similar results indicating that microcolumnar structure is quite sensitive to even minor perturbations in neuronal location.

3.5. Validity of the distance between microcolumns, P

An important question with respect to measures of the distance between microcolumns *P* in our calculation is the validity of such a measure in light of both the random orientation of the cut sections relative to microcolumns and the shrinkage of the cut section when fixed to a slide that effectively converts the three-dimensional *XYZ* positions into an *XY* set (i.e. *Z* is collapsed by shrinkage). As a result, one must consider the extent to which measurements of *P* may not be unbiased estimates of the true value of distances between microcolumns. To address this, we created a three-dimensional simulation that demonstrates that the true distance between microcolumns can be adequately approximated by the calculated *P*. For this simulation we place ideal microcolumns in a box rising from the vertices of a triangular lattice (Fig. 8A) whose lattice spacing *s* is the control variable. As shown in Fig. 8B, for each value of *s* we "cut" a 30 μm thick slab by selecting microcolumns in a way that mimics the way tissue sections are really cut. By changing the orientation angle of the cut "section" relative to the lattice, we are able to average

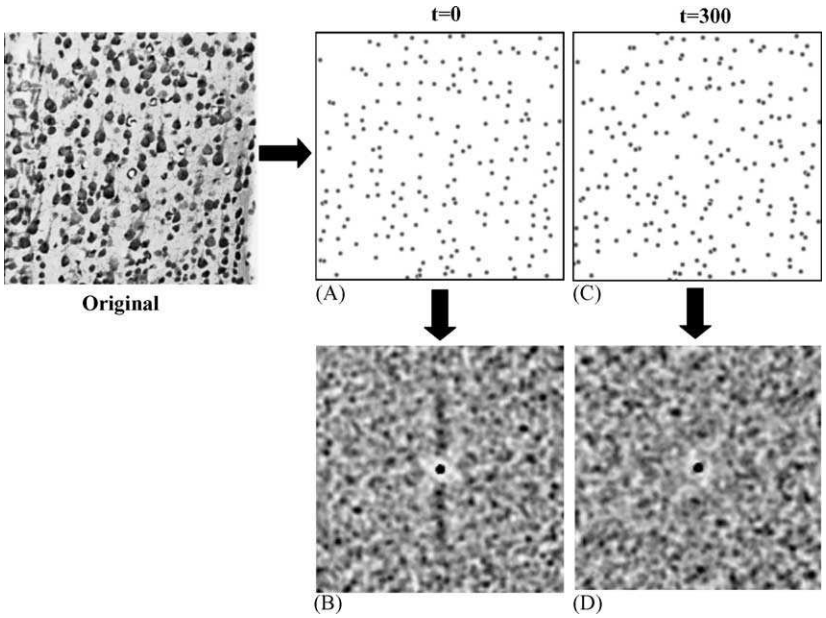

Fig. 7. Computer simulation in which positions of neurons are altered following the rules of random walk motion around the neuronal origins. (A) The simulation uses as the starting point ($t = 0$) the coordinates of the neurons from a digitized tissue image (left). The corresponding initial density map shows microcolumnar structure (B). (C) The neuronal positions after $t = 300$ random walk steps, with an average step size of 0.3 μm, have been displaced on average by a distance of the order of one neuronal diameter. The corresponding density map for the final configuration lacks microcolumnar structure (D).

over many samples. For each "section" we collapse the microcolumns (*Z* shrinkage) into a two-dimensional "slide" and calculate the density maps in the usual way (e.g. Fig. 8C). We generated a total of eight sections of 30 μm thickness (each at random orientational angles) for five different lattice spacings *s*. The results for *P* are shown in Fig. 8D as a function of lattice spacing *s*, in which a linear behavior is observed for small *s*, but as *s* increases toward the thickness of our sections, estimates of *P* flatten. Because *s* is the true distance between microcolumns, Fig. 8D allows the "translation" of a measure of *P* into an estimate of the true three-dimensional distance between microcolumns. For the values of *P* found in the areas studied in this paper ($P_{ave} \approx 26$ μm), Fig. 8D translates this distance to about 28 μm as the real distance between microcolumns in the tissue. Although this simulation was carried out using a triangular lattice, similar behavior to Fig. 8D would be obtained for different lattice geometries, as averaging over many slabs decreases the dependence of the results on the specific geometry.

3.6. Validity of L as a comparative measure of microcolumnar length

Since microcolumns are oriented perpendicularly to the curvilinear cortical surface, it would be ideal to cut sections exactly perpendicular to the surface, i.e. "vertically". While

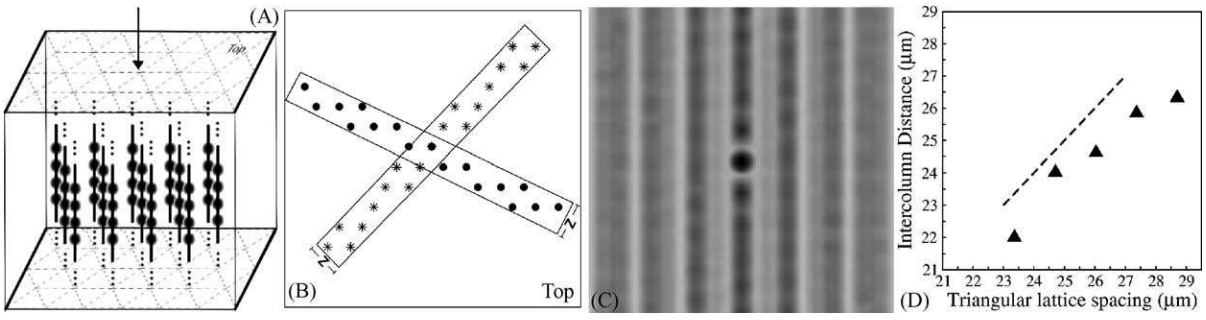

Fig. 8. Computer simulation of the effects of tissue shrinkage on the calculated values of the distance between microcolumns *P*. (A) We construct a periodic three-dimensional columnar neuronal structure inside a box by putting vertical columns rising up from the vertices of a triangular lattice with spacing *s*. To obtain smoother vertical columns in the density maps, we assign a random value in the range of 10–25 μm to the vertical distance between neurons. (B) We then select columns by "cutting" vertical slabs of 30 μm in thickness, mimicking the way tissue is cut in real brain. In the example shown (B) there is a slab cut at 154° with 17 columns (filled circles) and one at 46° with 19 columns (stars). (C) After we "cut" each slab, we project the three-dimensional coordinates of the simulated neurons into the two-dimensional plane of the slabs, obtaining images that mimic real tissue slices after shrinkage in the *Z* direction. We then calculate density maps (one per slab) in the same way as described in the text. (D) For all density maps, we measure *P* for different *s* and plot them as a function of *s*. The dashed line indicates the ideal dependence of *P* in *s* obtained for infinitesimally thin slabs.

this can be done on tiny blocks, it is impossible to do if one wishes to analyze complete serial sections through the entire hemisphere or any significant part of it. Still, it is clear that across all slices in a whole brain series (typically around 200), many sections will cut tangentially through microcolumns. Thus, the length of microcolumns *L* reported above is only an effective (as opposed to true) measure of the microcolumnar lengths, as microcolumns will seldom be contained in their entirety within one slice. Instead they will be truncated at differing lengths according to their relative orientation to the tissue section. But considering that microcolumns in all coronal sections across all cases are subject to similar truncation due to their orientation variability (i.e. similar probability of truncation), the effective value for *L* is still a useful quantity for comparing regions across similarly sectioned cases.

4. Discussion

4.1. Summary

The proposed density map method allows quantification of microcolumns in cortical areas that differ dramatically in visually apparent microcolumns. The obtained measures of microcolumnarity demonstrate both similarities and differences in microcolumnarity of these different regions. Thus, area TE contains the strongest microcolumns as indicated by *S*, while Area 46 and TL are similar to each other. Also, the length of microcolumns *L* has decreasing values for TE, 46, and TL, respectively. In contrast, the width of microcolumns *W* and distance between microcolumns *P* are similar across all areas. In addition, the degree of microcolumnar periodicity *T* is unchanged and is not significantly above the background for all areas indicating a loose positional organization of microcolumns.

4.2. Validation and consequences

The use of a semi-automated neuronal detection method to generate the required *XY* positional data is validated by directly comparing this method with manual marking and then by comparing the resulting density maps. Although the particular choice of neuronal detection method is not essential as other methods may be used (such as the *NIH Image* package or various commercial products), we show that at least 87% accuracy in the neuronal detection is sufficient to quantify and obtain relevant information about microcolumnarity in the brain.

The values for *S*, which assesses the *strength of the microcolumns*, indicate that this parameter increases as we move from the “limbic” cortex of the parahippocampal gyrus (TL) to the association cortices of the frontal (46) and temporal (TE) lobes. Since higher values of *S* indicate that there are more neurons within a given microcolumn this likely reflects fundamental functional capacities of the microcolumn.

In contrast, the weak values for *T*, which assesses the *periodicity of the microcolumns*, likely indicates that microcolumns are not specifically positioned with respect to other individual microcolumns as are atoms in a crystal, but instead resemble the organization of atoms found in liquids or gases with weaker positional correlations. These loose correlations in microcolumnar positions are also reflected in values for *P*, which assess the *distance between microcolumns*, reflecting the fact that, on average, there is no appreciable distinction of microcolumnar positions for the three radically different areas examined here (46, TL and TE). The relatively similar values of *W*, which assess the *width of the microcolumns*, may indicate that lateral positional correlations between neurons in the microcolumn are a property that may be shared in different areas in the cortex. The contrasting trends between *S* and both *P* and *W* may be due to the fact that while *S* depends on neuronal density, *P* and *W* only depend on the spatial arrangement of the microcolumns.

We have shown that our calculations of the distance between microcolumns *P* yield a sufficient estimate of the true distance despite the random orientation of tissue sections relative to that of the microcolumn and the shrinkage of the tissue that causes a two-dimensional collapse in the *Z* direction. Thus, the density map method can assess the three-dimensional character of microcolumnar arrangement using only two-dimensional data. From our calculations we conclude that corrections to the calculated *P* are accurate as long as the thickness of the samples are of the same order as the real microcolumnar distances. We have also demonstrated that even small random perturbations of neuronal position (on the order of one neuronal diameter) disrupt microcolumnarity and that the density map method is sufficient to detect such subtle alterations. To validate this point further, we have plans to address the three-dimensional character of microcolumns with respect to the measures of microcolumnarity by preparing thick plastic sections and manually acquiring complete three-dimensional data.

4.3. Other methods of analyzing microcolumns

A variant of the present density map method has been successfully applied to study alterations in microcolumnar organization in AD and LBD (Buldyrev et al., 2000) and has been generalized into a cross-correlation density map method to study the neurotoxic effect of fibrillar amyloid plaques on local neuronal density in AD (Urbanc et al., 2002). Independently, Buxhoeveden and colleagues have proposed a method to quantify microcolumnar organization of neurons in the cortex and used this to characterize microcolumnar disruption in schizophrenia (Buxhoeveden et al., 2000b), dyslexia (Casanova et al., 2002b), autism (Casanova et al., 2002a), and Down’s syndrome (Buxhoeveden et al., 2002b) and to identify significant differences in microcolumnar organization across species (Buxhoeveden et al., 2001; Buxhoeveden et al., 2002a).

In their method, neuron positions are obtained using the NIH Image software package. Then, they orient their images such that any apparent microcolumns align with the vertical axis. Next, they replace each neuron by a Gaussian density distribution and then project the sum of all distributions (one per neuron) onto the horizontal axis. This projected sum of distributions displays minima that are taken as the space between microcolumns and maxima that are taken as the centers of microcolumns. Then, they discard microcolumns that are by visual inspection truncated (Buxhoeveden et al., 2000a). From the surviving microcolumns they obtain the following measures: (i) a mean absolute deflection, (ii) an interval width, (iii) a column distance (horizontal distance between the centers of microcolumns), (iv) a vertical dispersion ratio, (v) a relative dispersion ratio, (vi) a neuropil space, (vii) a cell spacing, and (viii) a total path-length ratio.

Some of their quantities (mean absolute deflection, interval width, column distance, vertical dispersion ratio, relative dispersion ratio, and neuropil space) are closely related to our measures. Their mean absolute deflection is equivalent to *W*. Both, the interval width and the column distance are equivalent to *P* (our method does not distinguish between the two). Their vertical dispersion ratio measures the vertical dimension of the microcolumn relative to its horizontal dimension and is thus equivalent to the ratio of *L* to *W*. Their neuropil space can be calculated by subtracting *W* from *P*. Their relative dispersion ratio, a measure of the ratio of the vertical length of the cell cluster over its width to the height of the ROI over its width, can be calculated from our quantities as $LP/(WH)$, where *H* is the length of the ROI. Their other quantities, the cell spacing and the total path-length ratio, give additional information about the placement of an individual neuron inside each microcolumn. While our density map method contains information about the average spacing between the cells in the microcolumn, it cannot measure the total path-length ratio due to its statistical nature (the density map is an average over many neuronal *XY* sets).

On the other hand, the statistical nature of our density map approach has several advantages over the alternative method (Buxhoeveden et al., 2000a). Our density map method only needs the *XY* and/or the *XYZ* positions of the cells under study as input data without any assumptions regarding the internal structural organization of cortex, angular orientations, or radial distribution of cells. As such, our method can be applied to any region, even the ones without any apparent microcolumnar organization, which reduces the subjectivity of the analysis. The alternative method precludes analysis of regions of weak microcolumnar order in which a high noise-to-signal ratio may not allow for a clear distinction between maxima and minima of the sum of the Gaussian distributions, necessary to separate neighboring microcolumns. Also, in our method, slight imperfections (such as an occasional discontinuity of a microcolumn) are averaged out and do not significantly influence the final quantities. Our method provides two new quantities, *S* and *T*, that cannot be easily obtained by the alternative method that does not consider local neuronal densities. This is important in light of the results above, in which *S* may uniquely differentiate different cortical regions.

But this raises several other questions. First, is microcolumnarity relatively constant within a cortical region of a given subject or are there heterogeneities? Second, how does microcolumnarity change at the cytoarchitectonic transition zones? For example, Schleicher et al. (1999) used a densitometric method to quantify neuronal densities perpendicular to the cortical surface across these borders. It would be interesting to see how our method compares. Such studies require more exhaustive sampling of cortical spatial organization and to accomplish this we are developing a "moving window" analysis program to obtain continuous measures of microcolumnarity across large expanses of cortex. Once fully automated our method will be capable of quantifying measures of microcolumnarity in different cortical areas across a variety of experimental or pathological conditions (e.g. development, aging, neurodegenerative disease, developmental disorders, etc.) where the alternative method would be time-consuming, difficult, or impossible to apply.

4.4. Caveats and limitations

In order to minimize the effect that the curvature of tissue may have on the angular orientation of its inherent microcolumns, within the areas analyzed we have chosen regions that are relatively flat and away from the extreme curvatures of the lip or fundus of any sulci. This, of course, excludes from our calculations those regions that exhibit large variability in microcolumnar angular distributions as microcolumns "fan" out or in at tissue turns. We are currently working on expanding our algorithms to automatically convert neuronal positions in curved tissue from a polar coordinate system (natural to curved space) to a rectangular coordinate system that the density map requires. Once this is achieved, we will also be able to apply our density map calculations as described here to highly curved regions. In addition, our estimate of columnar width (*W*) is statistically determined using the center point of the neurons. Hence, this will be an underestimate of microcolumnar width determined visually by at least one neuronal diameter (i.e. half on each side). In principle, it may be possible to derive correction factors based on average neuronal diameters but this would require careful validation.

4.5. Conclusions

We have demonstrated that using only *XY* coordinates obtained manually or with semi-automated neuron detection methods, we can obtain a statistical characterization of the "average" microcolumnarity of any relatively flat region of the cortex using only 30 μm thick frozen sections stained with thionin. We have also shown that even without loss of neurons, very small alterations in neuronal positions (averaging one neuronal diameter) could lead to detectable loss of measures of microcolumnarity even in the highly microcolumnar area TE. Thus, it is plausible that microcolumnar

structure may provide a window into cortical organization and plasticity even in the adult brain that is quite dynamic in many ways. For example, synapses can expand and retract on a time scale of minutes to hours in response to LTP (e.g. Leuner et al., 2003; Lynch, 2004; Lambrecht and LeDoux, 2004), as well as days to weeks in response to hormonal manipulations (Weeks, 2003). It is also clear that dendrites can sprout or regress (e.g. Weeks, 2003; Grill and Riddle, 2002), and there is growing evidence that even in the adult brain new neurons are generated and while controversial, may actually migrate within the brain and integrate into circuits over the course of weeks to months (e.g. Shors et al., 2001). Since our density map method is able to detect subtle differences in neuronal positional arrangements, it is sensitive enough to detect and quantify subtle changes in microcolumns that may result from such dynamic changes in the context of development, aging, and neuropathology as well as between areas and across species. As such, assessments of microcolumns may provide an important window through which to view, on a global and regional basis, subtle changes in neuronal spatial relationships in health and disease.

Acknowledgments

This work was supported by grants from the National Institutes of Health: P01-AG00001, T32-AG00277, R03-AG024633, and P51-RR000165, and a grant from the Memory Ride Foundation.

Appendix A. Supplementary data

Supplementary data associated with this article can be found, in the online version, at doi:10.1016/j.jneumeth.2004.09.005.

References

Blatt GJ, Rosene DL. Organization of direct hippocampal efferent projections to the cerebral cortex of the Rhesus monkey: projections from CA1, prosubiculum and subiculum to the temporal lobe. J Comp Neurol 1998;392:92–114.

Blatt GJ, Pandya DN, Rosene DL. Parcellation of cortical afferents to three distinct sectors in the parahippocampal gyrus of the rhesus monkey: an anatomical and neurophysiological study. J Comp Neurol 2003;466(2):161–79.

Brodmann K. Vergleichende Lokalisationslehre der Grosshirnrinde. Leipzig, Germany: Barth; 1909.

Buldyrev SV, Cruz L, Gomez-Isla T, Gomez-Tortosa E, Havlin S, Le R, Stanley HE, Urbanc B, Hyman BT. Description of microcolumnar ensembles in association cortex and their disruption in Alzheimer and Lewy body dementias. Proc Natl Acad Sci 2000;97(10):5039–43.

Buxhoeveden D, Lefkowitz W, Loats P, Armstrong E. The linear organization of cell columns in human and nonhuman anthropoid Tpt cortex. Anat Embryol 1996;194:23–36.

Buxhoeveden DP, Switala AE, Roy E, Casanova MF. Quantitative analysis of cell columns in the cerebral cortex. J Neurosci Methods 2000a;97:7–17.

Buxhoeveden D, Roy E, Switala A, Casanova MF. Reduced interneuronal space in schizophrenia. Biol Psychiatry 2000b;47:681–3.

Buxhoeveden DP, Switala AE, Roy E, Litaker M, Casanova MF. Morphological differences between minicolumns in human and nonhuman primate cortex. Am J Phys Anthropol 2001;115:361–71.

Buxhoeveden DP, Switala AE, Litaker M, Roy E, Casanova MF. Lateralization of minicolumns inhuman planum temporale is absent in nonhuman primate cortex. Brain Behav Evol 2002a;57:349–58.

Buxhoeveden D, Fobbs A, Roy E, Casanova M. Quantitative comparison of radial cell columns in children with Down's syndrome and controls. J Intellect Disabil Res 2002b;46:76–81.

Buxhoeveden DP, Casanova MF. The minicolumn and evolution of the brain. Brain Behav Evol 2002a;60:125–51.

Buxhoeveden DP, Casanova MF. The minicolumn hypothesis in neuroscience. Brain 2002b;125:935–51.

Calvin WH. Cortical columns, modules, and hebbian cell assemblies. In: Arbib MA, editor. The handbook of brain theory and neural networks. MIT Press: Cambridge, MA; 1995. p. 269–72.

Casanova MF, Buxhoeveden DP, Switala AE, Roy E. Minicolumnar pathology in autism. Neurology 2002a;58:428–32.

Casanova MF, Buxhoeveden DP, Cohen M, Switala AE, Roy EL. Minicolumnar pathology in dyslexia. Ann Neurol 2002b;52:108–10.

Damasio AR, Damasio H, Van Hoesen GW. Prosopagnosia: anatomic basis and behavioral mechanisms. Neurology 1982;32(4):331–41.

Goldman PS, Rosvold HE. Localization of function within the dorsolateral prefrontal cortex of the rhesus monkey. Exp Neurol 1970;27:291–304.

Goldman PS, Rosvold HE, Vest B, Galkin TW. Analysis of the delayed alternation deficit produced by dorsolateral prefrontal lesions in the rhesus monkey. J Comp Physiol Psychol 1971;77:212–20.

Goldman-Rakic PS. Topography of cognition: parallel distributed networks in primate association cortex. Ann Rev Neurosci 1988;11:137–56.

Grill JD, Riddle DR. Age-related and laminar-specific dendritic changes in the medial frontal cortex of the rat. Brain Res 2002;937(1–2):8–21.

Herndon JG, Moss MB, Rosene DL, Killiany RJ. Patterns of cognitive decline in aged rhesus monkeys. Behav Brain Res 1997;87:25–34.

Hubel DH, Wiesel TN. Shape and arrangement of columns in cat's striate cortex. J Physiol 1963;165:559–68.

Hubel DH, Wiesel TN. Anatomical demonstration of columns in the monkey striate cortex. Nature 1969;221(182):747–50.

Hubel DH, Wiesel TN. Functional architecture of macaque visual cortex. Proc R Soc Lond B 1977;198:1–59.

Jones EG. Microcolumns in the cerebral cortex. Proc Natl Acad Sci 2000;97(10):5019–21.

Lambrecht R, LeDoux J. Structural plasticity and memory. Nat Rev Neurosci 2004;5:45–54.

Leuner B, Falduto J, Shors TJ. Associative memory formation increases the observation of dendritic spines in the hippocappus. J Neurosci 2003;23:659–65.

Leventhal AG, Wang Y, Pu M, Zhou Y, Ma Y. GABA and its agonists improved visual cortical function in senescent monkeys. Science 2003;300:812–5.

Lynch MA. Long-term potentiation and memory. Physiol Rev 2004;84:87–136.

Moore TL, Killiany RJ, Herndon JG, Rosene DL, Moss MB. Impairment in abstraction and set shifting in aged Rhesus monkeys. Neurobiol Aging 2003;5717:1–10.

Moore TL, Killiany RJ, Rosene DL, Prusty S, Hollander W, Moss MB. Impairment of executive function induced by hypertension in the rhesus monkey (*Macaca mulatta*). Behav Neurosci 2002;116(3):387–96.

Mountcastle VB. Modality and topographic properties of single neurons of cat's somatic sensory cortex. J Neurophysiol 1957;20:408–34.

Mountcastle VB. The columnar organization of the neocortex. Brain 1997;120:701–22.

Mountcastle VB. Untitled-introduction. Cereb Cortex 2003;13(1):2–4.

Peters A, Morrison JH, Rosene DL, Hyman BT. Feature article: are neurons lost from the primate cerebral cortex during normal aging? Cereb Cortex 1998;8(4):295–300.

Petrides M, Pandya DN. Comparative architectonic analysis of the human and macaque frontal cortex. In: Grafman J, Boller F, editors. Handbook of neuropsychology. Amsterdam: Elsevier A Science Publisher BV; 1994.

Petrides M. Dissociable roles of mid-dorsolateral prefrontal and anterior inferotemporal cortex in visual working memory. J Neurosci 2000a;20:7496–503.

Petrides M. The role of the mid-dorsolateral prefrontal cortex in working memory. Exp Brain Res 2000b;133:44–54.

Purves D, Riddle DR, LaMantia AS. Iterated patterns of brain circuitry (or how the cortex gets its spots). Trends Neurosci 1992;15:362–8.

Rosene DL, Roy NJ, Davis BJ. A cryoprotection method that facilitates cutting frozen sections of whole monkey brains for histological and histochemical processing without freezing artifact. J Histochem Cytochem 1986;34(10):1301–15.

Saleem KS, Tanaka K, Rockland KS. Specific and columnar projection from Area TEO to TE in the Macaque inferotemporal cortex. Cerebral Cortex 1993;3:454–64.

Schleicher A, Amunts K, Geyer S, Morosan P, Zilles K. Observer-independent method for microstructural parcellation of cerebral cortex: a quantitative approach to cytoarchitectonics. Neuroimage 1999;9:165–77.

Schmolesky MT, Wang Y, Pu M, Leventhal AG. Degradation of stimulus selectivity of visual cortical cells in senescent rhesus monkeys. Nat Neurosci 2000;3(4):384–90.

Shors TJ, Miesegaes G, Beylin A, Zhao M, Rydel T, Gould E. Neurogenesis in the adult is involved in the formation of trace memories. Nature 2001;410:372–5.

Suzuki WA. The anatomy, physiology and functions of the perirhinal cortex. Curr Opin Neurobiol 1996;6(2):179–86.

Swindale NV. Is the cerebral cortex modular? Trends Neurosci 1990;13:487–92.

Szentagothai J. The module-concept in cerebral cortex architecture. Brain Res 1975;95:475–96.

Tanaka K. Columns for complex visual object features in the inferotemporal cortex: clustering of cells with similar but slightly different stimulus selectivities. Cereb Cortex 2003;13(1):90–9.

Tsao DY, Freiwald WA, Knutsen TA, Mandeville JB, Tootell RB. Faces and objects in macaque cerebral cortex. Nat Neurosci 2003;6(9):989–95.

Urbanc B, Cruz L, Sanders J, Hsiao Ashe K, Duff K, Stanley HE, Irizarry MC, Hyman BT. Neurotoxic effects of thioflavin S-positive amyloid deposits in transgenic mice and Alzheimer's disease. Proc Natl Acad Sci 2002;99(22):13990–5.

Van Hoesen GW, Solodkin A. Some modular features of temporal cortex in humans as revealed by pathological changes in Alzheimer's Disease. Cerebral Cortex 1993;3:465–75.

Vogt C, Vogt O. Die physiologische Bedeutung der architektonishcen Rindenfelderung auf Grund neuer Rindenreizungen. J Psychol Neurol 1919;25:399–429.

Von Bonin G, Bailey P. The neocortex of *Macaca mulatta*. Urbana, IL: University of Illinois Press; 1947.

von Economo C, Koskinas GN. Die Cytoarchitektonik der Hirnrinde des erwachsenen Menchen. Berlin: Springer; 1925.

Weeks JC. Thinking globally, acting locally: steroid hormone regulation of the dendritic architecture, synaptic connectivity and death of an individual neuron. Prog Neurobiol 2003;70(5):421–42.